LASER & PHOTONICS REVIEWS
www.lpr-journal.org

Frequency-Division Multiplexing Continuous Variable Quantum Dense Coding with Broadband Entanglement

Shaocong Liang, Jialin Cheng, Jiliang Qin, Jiatong Li, Yi Shi, Baiyun Zeng, Zhihui Yan, Xiaojun Jia,* Changde Xie, and Kunchi Peng*

Quantum dense coding (QDC) provides great potential for high-capacity quantum communication. However, it is highly demanded for practical applications to realize high-capacity QDC with multiple coded information. Here, a high-capacity QDC with multiple streams is reported in different channels simultaneously through frequency-division multiplexing (FDM). The broadband entangled state is generated from a pair of degenerate optic al parametric amplifiers with short cavity lengths. Based on the resultant broadband entanglement, multiple pieces of information coded using binary phase shift keying (BPSK) are transferred with the FDM method. As an experimental demonstration, four pieces of information composed of pseudo-random numbers are transmitted at a rate of 4 Mbit s^{-1} using BPSK encoding. The decoded bit error rate reaches 10^{-3}, which is an average 35-fold improvement compared with the classical scheme. Furthermore, it is possible to make full use of sideband resource for four different information by using orthogonal FDM. This scheme can be extended to more different information by directly increasing the FDM sideband subchannels, and opens an avenue to construct high-capacity quantum communication, while minimizing the cost of quantum resource.

1. Introduction

Quantum information technologies can enhance communication capacity beyond the reach of the classical approach with nonclassical resources, such as quantum teleportation,[1–4] entanglement-assisted communication,[5] quantum key distribution,[6–8] quantum secure direct communication,[9] quantum secret sharing[10–13] and quantum dense coding (QDC).[14–17] In QDC, the sender can transmit two bits of classical information to the receiver by sending one quantum bit; and then the receiver decodes the two classical bits by performing a joint Bell-state measurement. Thus, QDC has the potential to double channel capacity with the assistance of quantum entanglement. Experiential implementations of QDC have been demonstrated in different physical systems, such as photonic qubits,[16,18,19] nuclear magnetic resonance[20] and atomic system.[21,22] Besides the discrete variables, continuous variables (CV) offer an alternative approach for efficiently implementing QDC to enhance the channel capacity. This is due to the advantages of deterministic generation and measurement, as well as the compatibility with classical commercial fiber communication. CV QDC has good compatibility with the classical communication, such as quantum radio-frequency-over-light communication[23] which has potential for practical application. High-capacity quantum communication is one of the aims, and broadband quantum entanglement enables to enhance the rate of QDC. Thus, CV QDC is an essential element for high-capacity quantum communication.

The channel multiplexing technology provides an effective method to enhance capacity and reduce the cost of quantum resources. There is significant progress in channel multiplexing QDC, such as orbital angular momentum and sideband modes multiplexed QDC.[24–27] The orbital angular momentum of light has been used to achieve multiplexing, thereby increasing the capacity of communication links.[28–30] The fourfold channel multiplexing QDC has been demonstrated, in which the extracted four pairs of entangled sideband modes are exploited.[31] Despite the remarkable achievements in high-capacity quantum communication, it remains a challenge to realize high-capacity and practical quantum multichannel communication. Meanwhile, there is a common pursuit in the field to reduce the cost of quantum resources.

Here, we demonstrate a high-capacity QDC for multiple pieces of information coded of binary phase shift keying (BPSK)-coded information, where a broadband entangled state and frequency-division multiplexing (FDM) method employed. The exploitation of a broadband entanglement source holds promise for implementing high-capacity QDC. The broadband

S. Liang, J. Cheng, J. Qin, J. Li, Y. Shi, B. Zeng, Z. Yan, X. Jia, C. Xie, K. Peng
State Key Laboratory of Quantum Optics and Quantum Optics Devices
Institute of Opto-Electronics
Shanxi University
Taiyuan 030006, China
E-mail: zhyan@sxu.edu.cn; jiaxj@sxu.edu.cn
J. Qin, Z. Yan, X. Jia, C. Xie, K. Peng
Collaborative Innovation Center of Extreme Optics
Shanxi University
Taiyuan, Shanxi 030006, China

The ORCID identification number(s) for the author(s) of this article can be found under https://doi.org/10.1002/lpor.202400094

DOI: 10.1002/lpor.202400094

Einstein–Podolsky–Rosen (EPR) entangled state is prepared by coupling a pair of 1.3 μm quadrature squeezed states from two degenerate optical parametric amplifiers (DOPAs) with short lengths. Digital communication technology based on BPSK encoding has the advantages of strong noise immunity and low-frequency band occupancy, making it highly suitable for CV-QDC. Meanwhile, FDM offers an effective quantum communication approach to make full use of quantum subchannels in the sidebands of broadband entangled state.[32,33] In the experiment, we simultaneously implement BPSK encoding to encode four binary pseudo-random numbers with 4 Mbit s^{-1} in two different sideband channels, respectively. Quantum entanglement improves the signal-to-noise ratio (SNR) by reducing channel noise. FDM enables the encoding of multiple BPSKs in different subchannels in the sidebands of broadband entanglement, and all bit error rates (BERs) reach 10^{-3} with an average 35-fold reduction compared to the classical scheme. Furthermore, both orthogonal frequency division multiplexing (OFDM) and interleaved single carrier frequency division multiplexing (I-SCFDM) encoding schemes have been implemented in this system, and four different information with higher efficiency utilization of sideband resource have been demonstrated by using OFDM and I-SCFDM. Therefore, our experimental results satisfy both high rate and channel multiplexing while minimizing the cost of quantum resources.

2. The Principle

The quadrature amplitude and quadrature phase operators of the electromagnetic field are defined as $\hat{X} = \hat{a} + \hat{a}^{\dagger}$, $\hat{Y} = i(\hat{a}^{\dagger} - \hat{a})$, where $\hat{a}^{\dagger}(\hat{a})$ is the creation operator (annihilation operator). The coherent state and vacuum state are two minimum-uncertainty states with $\langle \delta^2 \hat{X} \rangle = \langle \delta^2 \hat{Y} \rangle = 1$. The classical limit established by the vacuum state is called the shot noise limit (SNL). Another class of minimum-uncertainty states is the squeezed state, where one quadrature exhibits less noise than the SNL, but the noise in the other quadrature must be greater to maintain the minimum-uncertainty condition. Two identical and independently amplitude-squeezed vacuum modes $\hat{A}$, $\hat{B}$ can be described as $\hat{X}_A = e^{-r}\hat{X}_A(0)$, $\hat{X}_B = e^{-r}\hat{X}_B(0)$, $\hat{Y}_A = e^{r}\hat{Y}_A(0)$, $\hat{Y}_B = e^{r}\hat{Y}_B(0)$, where the superscript (0) denotes the initial vacuum modes and r is the squeezing parameter. By coupling the two squeezed modes at a 50/50 beam splitter(BS) with a relative phase $\frac{\pi}{2}$ yields the two output modes $\hat{X}_{EPR1} = \frac{1}{\sqrt{2}}(e^{-r}\hat{X}_A(0) - e^{r}\hat{Y}_B(0))$, $\hat{Y}_{EPR1} = \frac{1}{\sqrt{2}}(e^{r}\hat{Y}_A(0) + e^{-r}\hat{X}_B(0))$, $\hat{X}_{EPR2} = \frac{1}{\sqrt{2}}(e^{-r}\hat{X}_A(0) + e^{r}\hat{Y}_B(0))$, $\hat{Y}_{EPR2} = \frac{1}{\sqrt{2}}(e^{r}\hat{Y}_A(0) - e^{-r}\hat{X}_B(0))$. Thus, the correlation variances between EPR1 and EPR2 can be obtained as

$$\begin{aligned} \left\langle \delta^2(\hat{X}_{EPR1} + \hat{X}_{EPR2}) \right\rangle &= \left\langle \delta^2(\hat{Y}_{EPR1} - \hat{Y}_{EPR2}) \right\rangle = 2e^{-2r} \\ \left\langle \delta^2(\hat{X}_{EPR1} - \hat{X}_{EPR2}) \right\rangle &= \left\langle \delta^2(\hat{Y}_{EPR1} + \hat{Y}_{EPR2}) \right\rangle = 2e^{2r} \end{aligned} \tag{1}$$

While the variances of EPR2 is

$$\left\langle \delta^2 \hat{X}_{EPR2} \right\rangle = \left\langle \delta^2 \hat{Y}_{EPR2} \right\rangle = \frac{1}{2}(e^{-2r} + e^{2r}) \tag{2}$$

FDM can be divided into multiple independent transmission channels within the bandwidth of EPR entanglement. Alice encodes multiple sets of classic information on each subchannel of EPR2 and sends it to Bob, the nth classical information is $a_s(\omega n) = \frac{1}{2}(x_s(\omega n) + i y_s(\omega n))$.

At Bob's station, EPR1 is coupled to EPR2 by a 50/50 BS with a relative phase π, these two output fields can be described by the operators $\hat{X}_1(\omega n) = \frac{1}{\sqrt{2}}(\hat{X}_{EPR1}(\omega n) + \hat{X}_{EPR2}(\omega n) + x_s(\omega n))$, $\hat{Y}_1(\omega n) = \frac{1}{\sqrt{2}}(\hat{Y}_{EPR1}(\omega n) + \hat{Y}_{EPR2}(\omega n) + y_s(\omega n))$, $\hat{X}_2(\omega n) = \frac{1}{\sqrt{2}}(\hat{X}_{EPR1}(\omega n) - \hat{X}_{EPR2}(\omega n) - x_s(\omega n))$, $\hat{Y}_2(\omega n) = \frac{1}{\sqrt{2}}(\hat{Y}_{EPR1}(\omega n) - \hat{Y}_{EPR2}(\omega n) - y_s(\omega n))$.

By performing balanced homodyne detection (BHD) on the two outputs separately, the decoded n-th subchannel SNR for a single user is

$$\begin{aligned} SNR_{X_{EPR2}}(\omega n) &= \frac{2\left\langle \delta^2 x_s(\omega n) \right\rangle}{e^{-2r} + e^{2r}} \\ SNR_{Y_{EPR2}}(\omega n) &= \frac{2\left\langle \delta^2 y_s(\omega n) \right\rangle}{e^{-2r} + e^{2r}} \end{aligned} \tag{3}$$

With the joint processing with entanglement, the decoded SNR for decoded information is

$$\begin{aligned} SNR_{QDCX}(\omega n) &= \frac{\left\langle \delta^2 x_s(\omega n) \right\rangle}{2e^{-2r}}, \\ SNR_{QDCY}(\omega n) &= \frac{\left\langle \delta^2 y_s(\omega n) \right\rangle}{2e^{-2r}}. \end{aligned} \tag{4}$$

Thus, in the ideal case, $(r \to \infty)$, the decoded SNR for a single user is $SNR_{X_{EPR2}}(\omega n) = SNR_{Y_{EPR2}}(\omega n) \to 0$, and no signal can be obtained; the decoded SNR for joint processing is $SNR_{QDCX}(\omega n) = SNR_{QDCY}(\omega n) \to \infty$.

Thus, the SNR of QDC will be obviously enhanced beyond the classical limit, due to the squeezed quantum noise, otherwise the information derived from one mode of entanglement will be merged in quantum noises.

3. Experimental Section

BPSK is a well-understood code approach to transfer practical formation, and was applied in this FDM-QDC scheme. BPSK method was applied to modulate multiple pieces of information onto multiple radio frequency (RF) subcarriers, and then the subcarriers were further modulated on entangled submode, shown in **Figure 1**. The schematic of FDM-QDC is shown in Figure 1a, in which N digital encoding could be simultaneously realized on quadrature amplitude and phase, and thus $2N$ different messages were encoded. The experimental setup is demonstrated in Figure 1b. The CV broadband EPR entanglement source was placed at the sender Alice. The broadband EPR entangled source was generated by coupling two broadband single-mode amplitude-squeezed states. Two broadband squeezed states were prepared using a pair of DOPAs (DOPA1 and DOPA2) characterized by identical geometric structures and optical parameters. Each DOPA configuration consisted of a 6-mm nonlinear periodically poled $KTiOPO_4$ crystal and a rear cavity mirror with a curvature radius of 50 mm, constituting a semi-monolithic standing wave cavity structure. With an equivalent cavity length of 1 cm

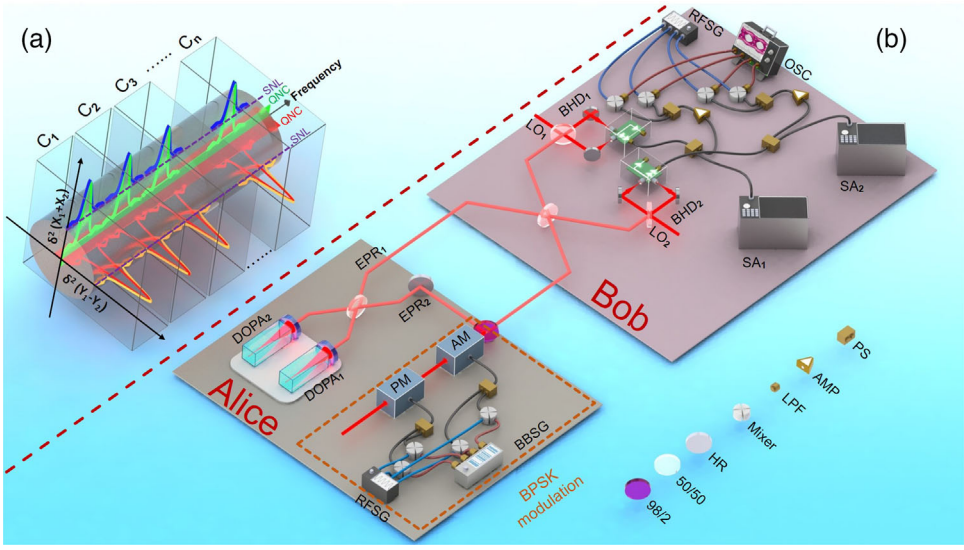

Figure 1. Schematic and experimental setup. a) The schematic of FDM-QDC. Broadband quantum entanglement channels reduce channel noise in each subchannel and increase channel capacity. QNC, quantum noise channel. b) The experimental setup. The broadband entangled state is generated by the 50/50 coupling of broadband quadrature amplitude squeezed light generated by two DOPAs working in parametric anti-amplification. Alice modulates the BPSK-encoded FDM intermediate frequency signal on the sideband mode of the quadrature amplitude and quadrature phase of the entangled submode EPR2. Alice sends two entangled beams to Bob for entanglement decoding. Bob measures the power noise spectra in the frequency domain and RF coherent decoding in the time domain to recover the sent binary information. DOPAs, degenerate optical parametric amplifiers; BBSG, base band signal generator; RFSG, RF signal generator; AM, amplitude modulator; PM, phase modulator; BHD, balanced homodyne detection; SA, spectrum analyzer; OSC, oscilloscope; LPF, low-pass filter; AMP, amplifier; PS, power splitter; LO, local oscillator; HR, high reflective mirror; 98/2, 98% reflective and 2% transmissive mirror; 50/50, 50% reflective and 50% transmissive mirror.

and a line width of ≈200 MHz, the DOPAs were operated in parametric anti-amplification states to produce two broadband amplitude-squeezed states. The two squeezed states were coupled to produce an EPR entangled state through a 50/50 BS, where the relative phase between two states is maintained at $\frac{\pi}{2} + k\pi$ (k is an integer).

Alice modulated four independent signals carrying information onto two sidebands of EPR2 using both amplitude and phase modulators. In the experiment, this was achieved by employing an auxiliary coherent beam, which was modulated with classical information and then coupled with EPR2 using a 98/2 BS. The bipolar non-return-to-zero code generated by the baseband signal generator and the RF subcarrier generated by the RF signal generator were up-converted by a mixer to generate a digital RF signal, which constitutes the fundamental process of BPSK encoding. The digital information sent at a bit rate of 4 Mbit s^{-1} consisted of several strings of binary pseudo-random sequences with a uniform distribution. The RF frequencies of the used subcarriers were 36 and 48 MHz, respectively. For amplitude (phase) encoding, the modulation amplitude of 36 and 48 MHz subcarrier were 80 mV (57 mV) and 90 mV (52 mV) respectively. The FDM-RF signal generated by the combination of two subcarriers was modulated on the displacement beam by the amplitude modulator and the phase modulator, respectively, and then coupled into EPR2. Subsequently, Alice sent EPR2 to Bob for entanglement decoding with the EPR1. At Bob's station, EPR1 was coupled to EPR2 by a 50/50 BS, and the entangled demodulated signal could be obtained by the BHD1 and BHD2. At the same time, Alice downconverted the information to FDM-RF. Amplified FDM-RF and then demultiplexed it by a power splitter. The baseband signal was recovered through coherent decoding, achieved by multiplying and low-pass filtering with local RF oscillations of the same frequency and phase as the RF carrier at Alice. The demodulated signal was captured using an oscilloscope and performs a sampling decision process to recover the binary code sent by Alice.

4. Results

To demonstrate high-capacity QDC with BPSK encoding, the power spectra of FDM-QDC are shown in **Figure** 2a,b and the emodulated signals and sampling decisions are shown in Figure 2c,d. Figure 2a,b shows the measured power spectra of quadrature phase and quadrature amplitude for the coherent state, the entangled state and the single submode EPR2, respectively. The orange traces and the purple traces in Figure 2a,b give the SNR results for the FDM-QDC scheme. For the quadrature-phase (amplitude), the SNRs are 9.5 ± 0.2 (10.0 ± 0.2) dB for the subcarriers at 36 MHz and 9.5 ± 0.2 (9.3 ± 0.2) dB for the subcarriers at 48 MHz, respectively. The green traces and the blue traces in Figure 2a,b give the SNR results for the coherent state scheme. For the quadrature phase (amplitude), the SNRs are 4.1 ± 0.1 (3.9 ± 0.2) dB for the 36 MHz subcarriers and 4.2 ± 0.2 (4.0 ± 0.1) dB for the 48 MHz subcarriers, respectively. The red traces and the black traces in Figure 2a,b can give the SNR results for the BHD measured. For the quadrature-phase (amplitude), the SNRs are −0.9 ± 0.1 (−0.5 ± 0.2) dB for the 36 MHz subcarriers and 0.2 ± 0.2 (−1.0 ± 0.2) dB for the 48 MHz subcarriers, respectively. To obtain the classic binary information sent by Alice, requires signal decoding and sampling decisions. As shown in Figure 1b,

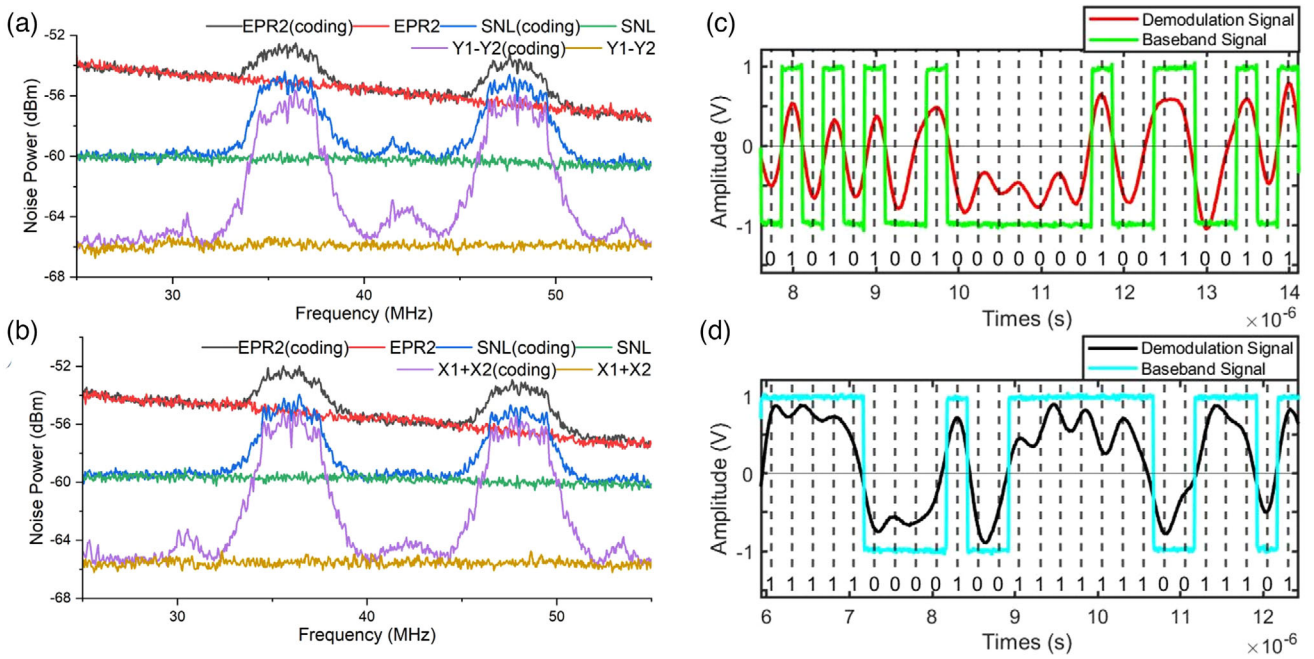

Figure 2. Power spectra and decoding process. a,b) Measured power spectra of quadrature phase and quadrature amplitude. The red trace and black trace represent the noise floor and encoded power spectrum of the entangled submode EPR2, respectively. The green trace and blue trace represent the noise floor (SNL) and encoded power spectrum of the coherent state, namely, the classical communication scheme, respectively. The orange trace and purple trace are the noise floor and encoded power spectrum of the EPR quantum correlation channel $\langle \delta^2(\hat{Y}_{EPR1} - \hat{Y}_{EPR2}) \rangle$ in a) and $\langle \delta^2(\hat{X}_{EPR1} + \hat{X}_{EPR2}) \rangle$ in b), respectively. c,d) Demodulated signals and sampling decisions for quadrature phase encodings at 36 and 48 MHz, respectively. The red (black) trace is the RF coherent decoding result of the 36 MHz (48 MHz) subcarrier. The green (cyan) trace is the original baseband signal of 36 MHz (48 MHz) subcarriers. The pulse lengths are 250 ns. The decision threshold is set at 0. If greater than 0, it is judged as 1, and if less than 0, it is judged as 0.

a signal amplifier is used to amplify the FDM-RF signal, and the 36 MHz (48 MHz) subcarriers signal is down-converted to the baseband by mixing with local RF signal. The output electrical signal is connected to an oscilloscope with a sampling rate of 250 MSa s^{-1} after passing through a 2 MHz low-pass filter. Taking the quadrature phase decoding and sampling decisions as an example, Figure 2c,d shows the process and results of sampling decisions. By means of this sampling decision process, the binary information encoded by Alice can be retrieved, and the measured BERs can be calculated. In this experiment, we accomplish the simultaneous encoding of four distinct pieces of information through BPSK encoding at a rate of 4 Mbit s^{-1}.

Meanwhile, BER is used to characterize the quality of QDC. BERs for different subcarriers in the quantum channel, the coherent-state channel, and the thermal-noise channel (single submode) are depicted in **Figure 3**. The light blue area represents the BER when the thermal submode EPR2 (with a noise level of $\frac{1}{2}(e^{2r} + e^{-2r})$) acts as the carrier and is detected in BHD. Meanwhile, the light orange area indicates the BER when quantum entanglement (with a noise level of $2e^{-2r}$) is introduced for the QDC scheme. In the FDM-QDC scheme, the BER is of the order of 10^{-3}. Specifically, for the quadrature phase (amplitude), the BERs are $(1.6 \pm 0.2) \times 10^{-3}((1.2 \pm 0.4) \times 10^{-3})$ for the subcarriers at 36 MHz and $(1.6 \pm 0.4) \times 10^{-3}((1.6 \pm 0.3) \times 10^{-3})$ for the subcarriers at 48 MHz, respectively. In contrast, for the coherent-state scheme or classical communication, the BER is in the order of 10^{-2}. For the quadrature phase (amplitude), the BERs are $(5.7 \pm 0.5) \times 10^{-2}((5.2 \pm 0.4) \times 10^{-2})$ for the subcarriers at 36 MHz and $(5.2 \pm 0.4) \times 10^{-2}((5.0 \pm 0.5) \times 10^{-2})$ for the subcarriers at 48 MHz, respectively. Considering the thermal carrier (single submode and BHD), the BER has an order of magnitude of 10^{-1}. Specifically, for the quadrature-phase (amplitude), the BERs are $(1.77 \pm 0.05) \times 10^{-1}((1.62 \pm 0.09) \times 10^{-1})$ for the subcarriers at 36 MHz and $(1.41 \pm 0.05) \times 10^{-1}((1.3 \pm 0.1) \times 10^{-1})$ for the subcarriers at 48 MHz, respectively. It is evident that the decoding BER achieves 10^{-3} due to the assistance of an EPR entanglement source, representing an average 35-fold reduction compared to the classical scheme. More significantly, the BER of a single submode is two orders of magnitude higher than the BER of the FDM-QDC scheme. This implies that the thermal noise of the entangled submode masks the signal. Therefore, the FDM-QDC scheme exceeds the corresponding classical scheme in terms of communication quality for digital communication with BPSK encoding. In this measurement, we simultaneously encoded four pieces of information on a pair of quadrature components with two subcarriers, but only two pieces of information are decoded with a quantum-enhanced BER that can reach 10^{-3}.

The communication performances of two practical FDM technologies, OFDM[34–36] and I-SCFDM[37–39] have been investigated for the BPSK-modulated QDC. **Figure 4a,b** is the power spectra of the quadrature phase and quadrature amplitude of used carriers at OFDM encoding and I-SCFDM encoding. For the two FDM encoding schemes, the modulation depth of the two subcarriers is the same, with a modulation amplitude of 70 mV loaded on the amplitude modulator

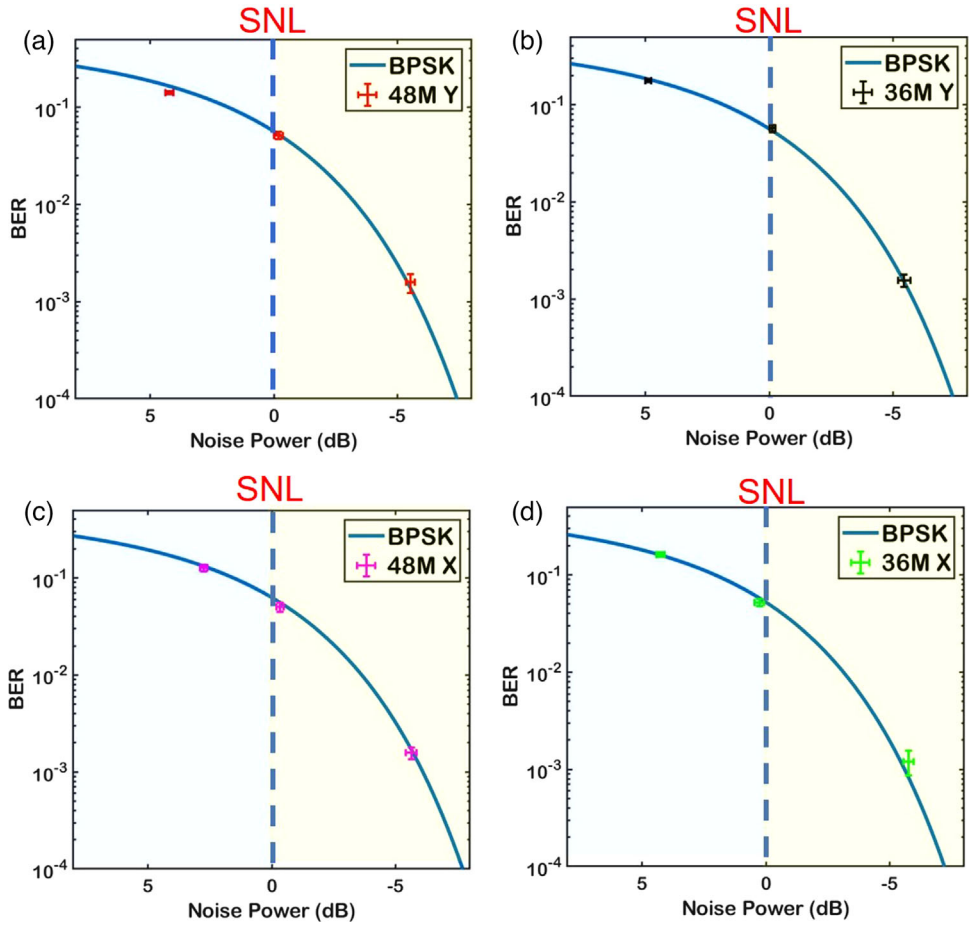

Figure 3. The BER analysis for the quantum channel, the coherent-state channel, and the thermal-noise channel (single submode) with the BPSK encoding. The blue traces are the theoretical BER curves. The dashed blue lines represent the corresponding SNLs. a,c) The red (magenta) dot represents the BER of the quadrature-phase (amplitude) decoded with the 48 MHz RF subcarrier. b,d) The black (green) dot represents the BER of the quadrature-phase (amplitude) decoded with the 36 MHz RF subcarrier.

and a modulation amplitude of 50 mV loaded on the phase modulator. For the quadrature phase, the SNRs are 7.2 ± 0.3 dB for the 44 MHz subcarriers and 6.9 ± 0.2 dB for the 48 MHz subcarriers, for the amplitude quadrature, the SNRs are 7.1 ± 0.2 dB for the 40 MHz subcarriers and 7.8 ± 0.1 dB for the 44 MHz subcarriers. The red traces and the blue traces in Figure 4a,b can give the SNR results for the I-SCFDM encoding scheme. For the quadrature phase, the SNRs are 7.5 ± 0.2 dB for the 40 MHz subcarriers and 6.6 ± 0.1 dB for the 48 MHz subcarriers. For the amplitude quadrature, the SNRs are 7.1 ± 0.2 dB for the 40 MHz subcarriers and 7.7 ± 0.2 dB for the 44 MHz subcarriers. Figure 4c,d is the BER of the quadrature phase and the quadrature amplitude with OFDM encoding and I-SCFDM encoding. The measured BER for the I-SCFDM approach is in good agreement with the experimentally determined BER, whereas the actual measured BER for the OFDM approach is 2–3 times higher than the theoretical BER. This higher BER in the OFDM approach may be attributed to the insufficient orthogonality of the two RF subcarriers. Despite the higher measured BER in the OFDM approach compared to that of I-SCFDM, it can still accommodate two different information codings. Consequently, four distinct binary information codings are achieved with a higher utilization rate within the entangled frequency bandwidth using OFDM.

5. Conclusion

In conclusion, we experimentally demonstrate the implementation of an FDM-QDC scheme using a broadband entangled state of light. Within the entanglement bandwidth, an improved SNR is attained for each subchannel compared to the classical limit and four BPSK modulations are realized simultaneously with the FDM method. The BER for each channel is significantly reduced and below the classical scheme. Furthermore, the OFDM modulation and the I-SCFDM modulation schemes are also implemented, and the FDM-QDC with a higher utilization rate within the entangled bandwidth is demonstrated by OFDM. The broadband entangled optical modes are the kernel quantum resource of QDC, which enables to obviously enhance the rate. Thus, the RF signal can be coded and decoded with higher rates, and the frequency-multiplex QDC has been demonstrated with such a broadband entangled state. Furthermore,

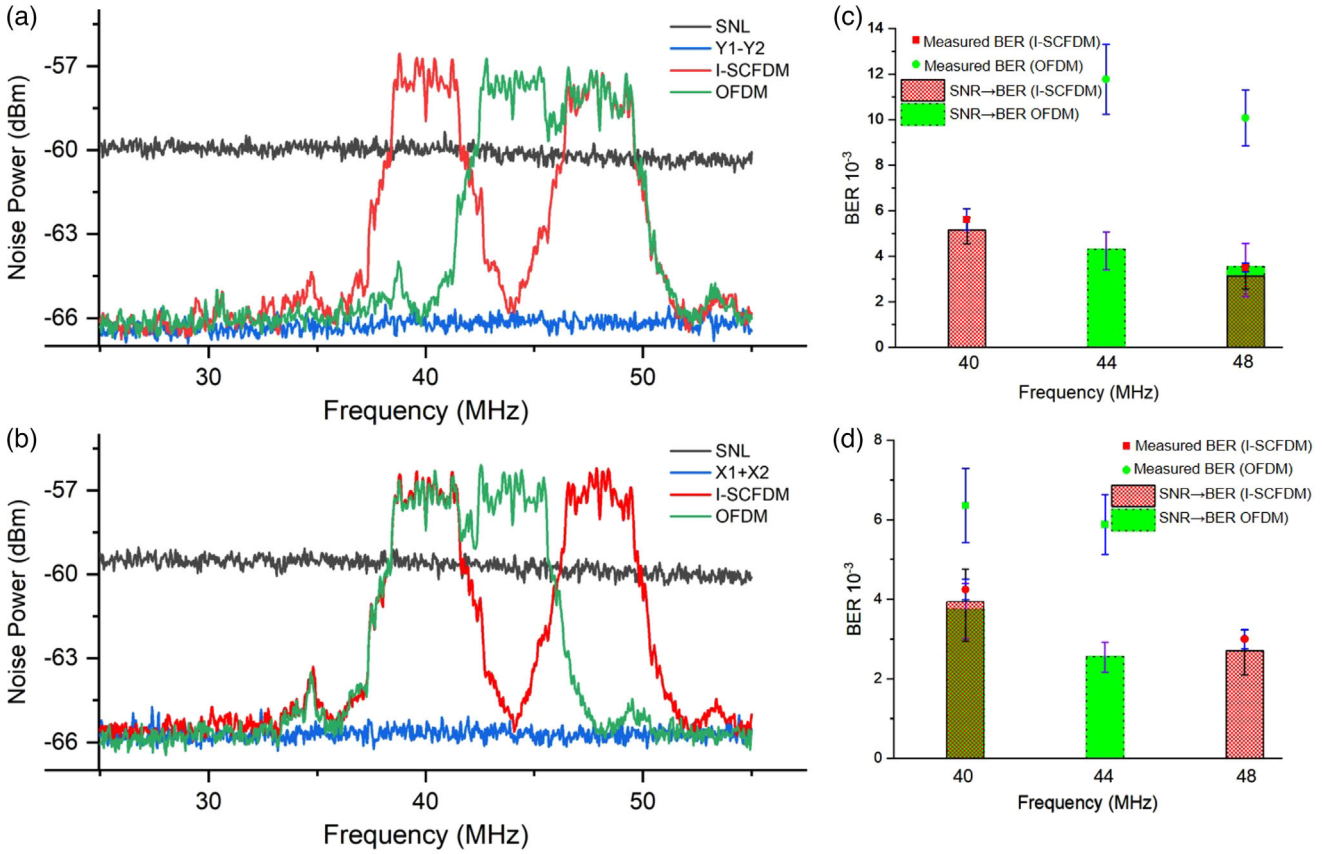

Figure 4. Measured BER in OFDM encoding and I-SCFDM encoding. a,b) The power spectra of quadrature phase and quadrature amplitude of four subcarriers at OFDM encoding and I-SCFDM encoding. The black trace is SNL and the blue trace is the quantum entanglement correlation noise. The red trace is the power spectrum of I-SCFDM encoding, and the green trace is the power spectrum of OFDM encoding. c,d) The BER of the quadrature phase and the quadrature amplitude with OFDM encoding and I-SCFDM encoding. The red (green) columns correspond to the theoretical BER calculated from the SNR obtained from the power spectrum of a,b) with the same frequencies. The red (green) points correspond to the measured BER at OFDM encoding and I-SCFDM encoding. The error bars are derived from ten consecutive BER measurements each based on 4×10^4 bits.

by increasing the squeezing bandwidth with low-loss periodically poled lithium niobate single-mode waveguide,[40] higher communication capacity and rate can be achieved. It is a long-standing goal to achieve secure quantum communication. Besides quantum key distribution, quantum secure direct communication is an alternative secure quantum communication protocol, which can transmit secret message with quantum entanglement instead of sharing the random key.[41,42] QDC is compatible with quantum secure direct communication and can be regarded as its second step.[22] After checking eavesdropping by choosing a fraction of entangled pairs to measure with a randomly chosen measuring basis, the partner entangled pairs are used to code and transfer the information with QDC approach.[43] This system can be potentially used to realize high-rate quantum secure direct communication.

Acknowledgements

S.L. and J.C. contributed equally to this work. This work was supported by the National Natural Science Foundation of China (Grants No. 61925503, No. 62122044, and No. 62135008), the National Key Research and Development Program of China (2022YFA1404500), the Program for the Innovative Talents of the Higher Education Institutions of Shanxi, the Program for the Outstanding Innovative Teams of the Higher Learning Institutions of Shanxi and the Fund for Shanxi "1331 Project" Key Subjects Construction.

Conflict of Interest

The authors declare no conflict of interest.

Data Availability Statement

The data that support the findings of this study are available from the corresponding author upon reasonable request.

Keywords

binary phase shift keying, continuous variable broadband entanglement, frequency-division multiplexing, quantum dense coding

Received: January 19, 2024
Revised: June 3, 2024
Published online:

[1] Z. Yan, J.-L. Qin, Z.-Z. Qin, X.-L. Su, X.-J. Jia, C.-D. Xie, K.-C. Peng, *Fundamental Res.* **2021**, *1*, 43.
[2] A. Furusawa, J. L. Sørensen, S. L. Braunstein, C. A. Fuchs, H. J. Kimble, E. S. Polzik, *Science* **1998**, *282*, 706.
[3] M. Huo, J. Qin, J. Cheng, Z. Yan, Z. Qin, X. Su, X. Jia, C. Xie, K. Peng, *Sci. Adv.* **2018**, *4*, eaas9401.
[4] H. Krauter, J. F. Sherson, E. S. Polzik, *Laser Photon. Rev.* **2010**, *4*, 685.
[5] S. Hao, H. Shi, W. Li, J. H. Shapiro, Q. Zhuang, Z. Zhang, *Phys. Rev. Lett.* **2021**, *126*, 250501.
[6] F. Grosshans, G. Van Assche, J. Wenger, R. Brouri, N. J. Cerf, P. Grangier, *Nature* **2003**, *421*, 238.
[7] Y. Zhang, Z. Chen, S. Pirandola, X. Wang, C. Zhou, B. Chu, Y. Zhao, B. Xu, S. Yu, H. Guo, *Phys. Rev. Lett.* **2020**, *125*, 010502.
[8] Y. Pi, H. Wang, Y. Pan, Y. Shao, Y. Li, J. Yang, Y. Zhang, W. Huang, B. Xu, *Opt. Lett.* **2023**, *48*, 1766.
[9] G. L. Long, X. S. Liu, *Phys. Rev. A* **2002**, *65*, 032302.
[10] A. Shamir, *Commun. ACM* **1979**, *22*, 612.
[11] S. Gaertner, C. Kurtsiefer, M. Bourennane, H. Weinfurter, *Phys. Rev. Lett.* **2007**, *98*, 020503.
[12] Y. Zhou, J. Yu, Z. Yan, X. Jia, J. Zhang, C. Xie, K. Peng, *Phys. Rev. Lett.* **2018**, *121*, 150502.
[13] J. Pinnell, I. Nape, M. de Oliveira, N. TabeBordbar, A. Forbes, *Laser Photon. Rev.* **2020**, *14*, 2000012.
[14] S. L. Braunstein, P. van Loock, *Rev. Mod. Phys.* **2005**, *77*, 513.
[15] C. H. Bennett, S. J. Wiesner, *Phys. Rev. Lett.* **1992**, *69*, 2881.
[16] K. Mattle, H. Weinfurter, P. G. Kwiat, A. Zeilinger, *Phys. Rev. Lett.* **1996**, *76*, 4656.
[17] X. Li, Q. Pan, J. Jing, J. Zhang, C. Xie, K. Peng, *Phys. Rev. Lett.* **2002**, *88*, 047904.
[18] B. P. Williams, R. J. Sadlier, T. S. Humble, *Phys. Rev. Lett.* **2017**, *118*, 050501.
[19] J. T. Barreiro, T.-C. Wei, P. G. Kwiat, *Nat. Phys.* **2008**, *4*, 282.
[20] X. Fang, X. Zhu, M. Feng, X. Mao, F. Du, *Phys. Rev. A* **2000**, *61*, 022307.
[21] T. Schaetz, M. D. Barrett, D. Leibfried, J. Chiaverini, J. Britton, W. M. Itano, J. D. Jost, C. Langer, D. J. Wineland, *Phys. Rev. Lett.* **2004**, *93*, 040505.
[22] W. Zhang, D.-S. Ding, Y.-B. Sheng, L. Zhou, B.-S. Shi, G.-C. Guo, *Phys. Rev. Lett.* **2017**, *118*, 220501.
[23] S. Liang, J. Cheng, J. Qin, J. Li, Y. Shi, Z. Yan, X. Jia, C. Xie, K. Peng, *Phys. Rev. Lett.* **2024**, *132*, 140802.
[24] M. Chen, N. C. Menicucci, O. Pfister, *Phys. Rev. Lett.* **2014**, *112*, 120505.
[25] J. Roslund, R. M. de Araújo, S. Jiang, C. Fabre, N. Treps, *Nat. Photonics* **2014**, *8*, 109.
[26] M. Pysher, Y. Miwa, R. Shahrokhshahi, R. Bloomer, O. Pfister, *Phys. Rev. Lett.* **2011**, *107*, 030505.
[27] S. Wengerowsky, S. K. Joshi, F. Steinlechner, H. Hübel, R. Ursin, *Nature* **2018**, *564*, 225.
[28] Y. Chen, S. Liu, Y. Lou, J. Jing, *Phys. Rev. Lett.* **2021**, *127*, 093601.
[29] J. Wang, J.-Y. Yang, I. M. Fazal, N. Ahmed, Y. Yan, H. Huang, Y. Ren, Y. Yue, S. Dolinar, M. Tur, A. E. Willner, *Nat. Photonics* **2012**, *6*, 488.
[30] N. Bozinovic, Y. Yue, Y. Ren, M. Tur, P. Kristensen, H. Huang, A. E. Willner, S. Ramachandran, *Science* **2013**, *340*, 1545.
[31] S. Shi, L. Tian, Y. Wang, Y. Zheng, C. Xie, K. Peng, *Phys. Rev. Lett.* **2020**, *125*, 070502.
[32] B. Hage, A. Samblowski, R. Schnabel, *Phys. Rev. A* **2010**, *81*, 062301.
[33] H. Song, H. Yonezawa, K. B. Kuntz, M. Heurs, E. H. Huntington, *Phys. Rev. A* **2014**, *90*, 042337.
[34] M. Al-Imari, P. Xiao, M. A. Imran, R. Tafazolli, in *2014 11th International Symposium on Wireless Communications Systems (ISWCS)*, **2014**, pp. 781–785.
[35] X. Yu, J.-C. Shen, J. Zhang, K. B. Letaief, *IEEE J. Sel. Top. Signal Process.* **2016**, *10*, 485.
[36] A. H. Azhar, T.-A. Tran, D. O'Brien, *IEEE Photon. Technol. Lett.* **2013**, *25*, 171.
[37] J. Zhou, Q. Wang, Q. Cheng, M. Guo, Y. Lu, A. Yang, Y. Qiao, *IEEE Photon. Technol. Lett.* **2018**, *30*, 165.
[38] V. K. Trivedi, P. Kumar, in *2017 IEEE International Conference on Communications Workshops (ICC Workshops)*, **2017**, pp. 785–790.
[39] C. Zhao, Y. Chen, S. Zhang, J. Li, F. Zhang, L. Zhu, Z. Chen, *Opt. Express* **2012**, *20*, 787.
[40] T. Kashiwazaki, T. Yamashima, K. Enbutsu, T. Kazama, A. Inoue, K. Fukui, M. Endo, T. Umeki, A. Furusawa, *Appl. Phys. Lett.* **2023**, *122*, 234003.
[41] L. Zhou, Y.-B. Sheng, *Sci. China-Phys, Mech. Astron.* **2022**, *65*, 250311.
[42] Y.-B. Sheng, L. Zhou, G.-L. Long, *Sci. Bull.* **2022**, *67*, 367.
[43] F.-G. Deng, G. L. Long, X.-S. Liu, *Phys. Rev. A* **2003**, *68*, 042317.